*J. Fluid Mech.* (2018), *vol.* 846, R3, doi:10.1017/jfm.2018.312

JFM RAPIDS
journals.cambridge.org/rapids

# Production of monodisperse microbubbles avoiding microfluidics

**Enrique S. Quintero**[1], **A. Evangelio**[1] **and J. M. Gordillo**[1,†]

[1]Área de Mecánica de Fluidos, Departamento de Ingenería Aeroespacial y Mecánica de Fluidos, Universidad de Sevilla, Avenida de los Descubrimientos s/n 41092, Sevilla, Spain

(Received 1 March 2018; revised 5 April 2018; accepted 6 April 2018;
first published online 3 May 2018)

Here we report the production of monodisperse microbubbles by taking advantage of the large values of both the pressure gradients and of the local velocities existing at the leading edge of airfoils in relative motion with a liquid. It is shown here that the scaling laws for the bubbling frequencies and the bubble diameters are identical to those found in microfluidics. Therefore, the metre-sized geometry presented here is a feasible candidate to circumvent the inherent problems of using micron-sized geometries in real applications – namely, wettability, the low productivity and the clogging of the microchannels by particles or other impurities.

**Key words:** drops and bubbles, microfluidics, micro-/nano-fluid dynamics

## 1. Introduction

Producing monodisperse micron-sized bubbles possesses countless applications in a number of industrial processes, such as water purification, water aeration, biomass processing, separation (Rosso, Larson & Stenstrom 2008; Garcia-Ochoa & Gomez 2009; Zimmerman *et al.* 2011), and also in medicine, where they are currently used in lithotripsy (Yoshizawa *et al.* 2009), as ultrasound contrast agents (UCAS) or for drug delivery purposes (Ferrara, Pollard & Borden 2007).

Many different processes in industry and medicine, like the ones enumerated above, demand a precise control over the diameters, $d_b$, over the production frequencies, $f_b$, and over the polydispersity index (PDI) of the bubbles produced. But the controlled mass production of monodisperse micron-sized bubbles – namely, those for which PDI $< 0.05$ and $d_b < 10^{-3}$ m – for real industrial and medical applications still constitutes a technological challenge (Rodríguez-Rodríguez *et al.* 2015). This is partly due to the fact that producing microbubbles is a process that very much differs from the analogous case of drop generation in air: while a continuous liquid stream fragments into drops because of the growth of capillary instabilities (Villermaux 2007;

† Email address for correspondence: jgordill@us.es

Eggers & Villermaux 2008), bubbles form as a consequence of the differences in pressure at the liquid side of the interface. Indeed, following the seminal contribution by Oguz & Prosperetti (1993), Rodríguez-Rodríguez *et al.* (2015) used a very simple model, based on the Rayleigh–Plesset equation for the time-varying bubble radius $R_b(t)$ and on the continuity equation, namely,

$$\rho_l \left( R_b \ddot{R}_b + \frac{3}{2}\dot{R}_b^2 \right) = \Delta p_{exit} - \frac{2\sigma}{R_b} - 4\mu_l \frac{\dot{R}_b}{R_b} \tag{1.1}$$

$$Q_g = \frac{\pi}{6} d_b^3 f_b, \tag{1.2}$$

to scale both $d_b$ and $f_b$ for several of the vast number of existing technologies aimed at producing bubbles in a controlled manner. In equation (1.1), $\Delta p_{exit}$ refers to the time-varying gas pressure at the nozzle exit relative to that in the liquid far away from the bubble, $Q_g$ is the gas flow rate and $\rho_l$, $\mu_l$ and $\sigma$ indicate, respectively, the liquid density, the liquid viscosity and the interfacial tension coefficient.

The reason why a number of technological alternatives have appeared in the literature to generate bubbles is that their production from the direct injection of a gas inside a stagnant liquid pool possesses two clear shortcomings, namely, the coalescence between neighbours and the fact that the diameters of the bubbles produced are much larger than the diameter of the injector. To overcome these disadvantages, the novel bubble generation techniques reported in the recent literature can be classified depending on the way $\Delta p_{exit}$ in (1.1) is controlled. For instance, Shirota *et al.* (2008) report a method in which $\Delta p_{exit}$ is forced to vary in time by exciting the gas stream acoustically, a fact that favours the rapid collapse of the neck of the growing bubble, and an analogous effect is achieved using the approach described in Zimmerman *et al.* (2011), where the gas flow rate and, consequently, the gas pressure at the exit orifice oscillates in time. But, $\Delta p_{exit}$ in (1.1) can also be controlled by changing the liquid pressure around the bubble using either a co-flow or a crossflow. This production method has become very popular since the advent of microfluidics, thanks to the ease of manufacturing narrow channels in polydimethylsiloxane (PDMS) (Garstecki *et al.* 2004; Hettiarachchi *et al.* 2007; Fu & Youguang 2015; Campo-Cortés, Riboux & Gordillo 2016).

In the technological approaches that resort on using a liquid flow to promote the formation of bubbles, $\Delta p_{exit}$ in (1.1) represents the pressure difference in a distance of the order of the length of the bubble namely, $\Delta p_{exit} = \nabla p\, d_b$, with $\nabla p$ the value of the local pressure gradient. Therefore, in the high-Reynolds-number limit and in the case where capillary stresses can be neglected, the inertial terms in (1.1) are balanced with the pressure difference $\Delta p_{exit}$,

$$\rho R_b \ddot{R}_b \sim \rho d_b^2 f_b^2 \sim \Delta p \sim \nabla p\, d_b \Rightarrow f_b \propto \sqrt{\frac{|\nabla p|}{\rho d_b}}. \tag{1.3}$$

Substituting $f_b$ in (1.3) into (1.2) yields the following expression for $d_b$:

$$d_b^3 \sqrt{\frac{|\nabla p|}{\rho d_b}} \propto Q_g \Rightarrow d_b \propto \left( \frac{Q_g}{\sqrt{|\nabla p|/\rho}} \right)^{2/5}. \tag{1.4}$$

Notice that the pair of equations (1.3)–(1.4) have been deduced assuming that $\Delta p_{exit}$ in (1.1) dominates overcapillarity; namely, if the local Bond number based on the

pressure gradient $\boldsymbol{\nabla} p$ is such that

$$\boldsymbol{\nabla} p\, d_b \gtrsim \frac{\sigma}{d_b} \Rightarrow \frac{\boldsymbol{\nabla} p\, d_b^2}{\sigma} \gtrsim 1 \Rightarrow d_b \gtrsim \left(\frac{\sigma}{\boldsymbol{\nabla} p}\right)^{1/2}. \tag{1.5}$$

If condition (1.5) is not fulfilled, the role played by the pressure gradient in the bubble generation process is negligible. Under these circumstances, if the outer flow is able to overcome the interfacial tension confinement forces, namely if the Weber number $We = \rho\, U^2\, d_g/\sigma \gtrsim 1$, with $d_g$ the diameter of the gas ligament from which bubbles are produced and $U$ the local liquid velocity where the gas is injected, a bubble is formed once its tip is convected downstream a distance proportional to $d_g$, so that capillarity can force the pinch-off of the gas thread (Gordillo, Sevilla & Martínez-Bazán 2007; Campo-Cortés *et al.* 2016); therefore,

$$f_b \propto \frac{U}{d_g}, \quad d_b \propto \left(\frac{Q_g\, d_g}{U}\right)^{1/3}, \tag{1.6a,b}$$

where use of equation (1.2) has been made.

In summary, provided that viscous effects are negligible and that the gas flow rate $Q_g$ is constant during the bubble formation process (Oguz & Prosperetti 1993), the frequency $f_b$ and the diameters $d_b$ of the bubbles produced can be predicted using either the pair of equations (1.3) and (1.4) or equations (1.6), depending on whether the condition in (1.5) is satisfied or not, irrespective of the way the local pressure gradient $\boldsymbol{\nabla} p$ and the local velocity $U$ are generated.

The reason why microfluidic geometries are used to produce microbubbles relies on the fact that the characteristic length scale of the channels and orifices, $L$, is of the order of tens of microns (Gañán-Calvo & Gordillo 2001). Indeed, under these circumstances, the diameter of the gas ligament, $d_g$, is very small and the associated pressure gradients, $|\boldsymbol{\nabla} p| \sim O(\rho U^2/L)$, are much larger than those produced in a stagnant liquid pool, namely $|\boldsymbol{\nabla} p| \gg \rho\, g$. Therefore, by virtue of (1.4), the diameters of the bubbles is reduced because the equivalent gravity produced by the flow field $|\boldsymbol{\nabla} p|/\rho \sim O(U^2/L)$ is orders of magnitude larger than $g$; see equations (1.3) and (1.4).

However, the use of microfluidic geometries possess two clear drawbacks for real applications: (i) the production rates are very low, a limitation which could be partially solved by multiplexing the geometry of the unit production cell; and (ii) the narrow channels are prone to clogging by solid particles or other impurities.

To circumvent the operating problems associated with the use of microchannels, here we present a method to massively produce monodisperse micron-sized bubbles avoiding the use of microfluidic geometries by injecting the gas at the leading edge of an airfoil of characteristic chord $c$ moving with a relative speed $U_\infty$ inside a liquid of density $\rho$. The reason behind this design is motivated by the fact that, in this region of an airfoil, the local liquid velocities are of the order of metres per second and much larger than $U_\infty$ and, in addition, the associated favourable pressure gradients are orders of magnitude larger than $\sim O(\rho U_\infty^2/c)$ and comparable to those in microfluidic devices for sufficiently large values of the angle of attack, $\alpha$, formed between the chord of the airfoil and the incident stream.

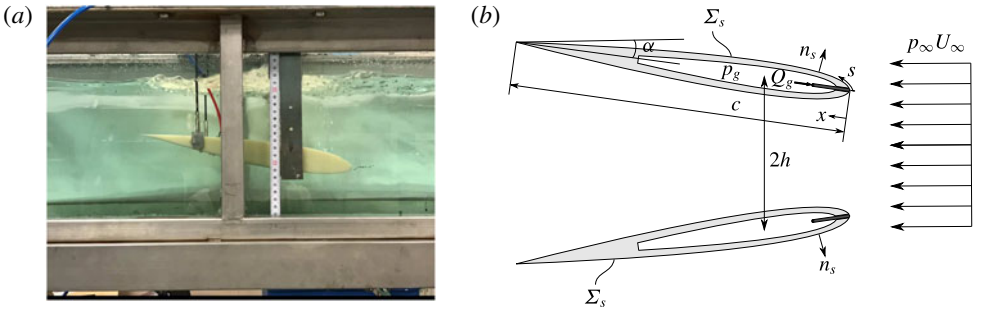


FIGURE 1. (*a*) Rectangular wing composed by NACA 0012 airfoils located inside the water tunnel at an angle of attack of $\alpha = 10°$. (*b*) Sketch of the hollow airfoil, where the pressurized chamber, the gas injection tube and the boundaries of the system (2.2) are shown. Here, $h$ indicates the airfoil distance to the wall.

## 2. Bubbling at the leading edge of an airfoil

Figure 1 shows a rectangular wing of span $b = 0.27$ m and chord $c = 0.3$ m composed of NACA 0012 airfoils (see, for example, Abbot & Von Doenhoff (1959) for details about the definition of the geometry of this common type of standardized lifting surface). The wing is immersed inside a square-section water tunnel of width $w = 0.3\ \text{m} \simeq b$ (see figure 1*a*); therefore, no wing tip vortices are created and the flow field is two-dimensional (i.e. the velocity vectors are contained in planes perpendicular to the span direction). The flow rate is controlled by varying the angular velocity of the impeller of a centrifugal pump and is measured using a particle tracking method. The gas is injected into the liquid from a pressurized reservoir located inside the airfoil to the different orifices placed at the leading edge region through injection tubes of length $l_t = 6 \times 10^{-2}$ m and inner diameter $d_t = 1.6 \times 10^{-4}$ m; see figure 1(*b*). Since the ratio $l_t/d_t \gg 1$, the flow resistance is large enough to keep the gas flow rate constant during the bubble formation process (Oguz & Prosperetti 1993). The gas flow rate, $Q_g$, is controlled using high-precision pressure regulators to fix the value of the gas pressure $p_g$ in figure 1(*b*). Experiments are visualized using a high-speed camera Phantom v710 operated at 10 000 fps. The focal distance is $\simeq$0.11 m and the final spatial resolution of the images captured is 20 $\mu$m pixel$^{-1}$.

Since bubbles are formed periodically, bubbling frequencies are determined from the analysis of the videos recorded. This is done measuring the time required for 20 bubbles to cross an imaginary line located downstream of the gas injection orifice. The gas flow rate could have been determined as a function of the pressure difference $p_g - p_\infty$ but, since the Reynolds number $Re_t$ characterizing the flow inside the injection tubes is such that $Re_t d_t/l_t = Q_g/(\nu_g\, l_t) \sim O(1)$, with $\nu_g = 1.5 \times 10^{-5}$ m$^2$ s$^{-1}$ the kinematic viscosity of the gas, the gas velocity profile inside the injection tubes is not Poiseuille-like and we found that the most precise way to calculate $Q_g$ is to make use of (1.2) with $d_b$ also measured from the experimental images. The local liquid velocity and the local pressure gradient at the gas injection orifices, where bubbles are generated, are calculated numerically, using potential flow theory.

Indeed, since vorticity is confined to thin boundary layers if the flow around the airfoil is not separated (i.e. for angles of attack verifying the condition $\alpha < \alpha^*$, with $\alpha^* \approx 15°$ the angle above which the boundary layer is no longer attached), the velocity

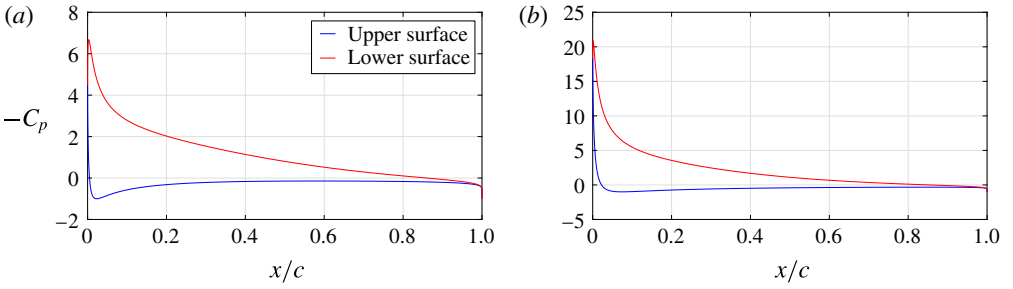


FIGURE 2. Variation of the pressure coefficient with the dimensionless distance to the leading edge, $-C_p(x/c)$, at both sides of the NACA 0012 airfoil sketched in the top part of figure 1(*b*) for two different values of the angle of attack: (*a*) $\alpha = 6^\circ$ and (*b*) $\alpha = 12^\circ$. Notice that the maximum values of $-C_p$ exhibited by the curves in (*a*) and (*b*) are larger than the ones corresponding to the case of isolated airfoils: indeed, for isolated airfoils, the maximum values of $-C_p$ for $\alpha = 6^\circ$ and $\alpha = 12^\circ$ are, respectively, 2.7 and 8.6. Our design takes advantage of the geometrical arrangement in figure 1 to increase the values of both the suction peak and of the pressure gradient at the leading edge of the airfoil.

field can be expressed as

$$\boldsymbol{v} = \nabla\phi, \tag{2.1}$$

with $\phi$ the velocity potential satisfying the Laplace equation, subjected to the zero normal velocity condition at the airfoil surface $\Sigma_s$ and at the wall, this latter boundary condition being satisfied using the method of images as sketched in figure 1(*b*), and to the boundary condition at infinity, namely,

$$\nabla^2\phi = 0, \quad \nabla\phi \cdot \boldsymbol{n} = 0 \quad \boldsymbol{x} \in \Sigma_s, \quad \nabla\phi \to \boldsymbol{U}_\infty \quad |\boldsymbol{x}| \to \infty. \tag{2.2a–c}$$

The numerical solution to the system (2.2), which also needs to satisfy the so-called Kutta condition – i.e. that the flow cannot turn around the airfoil trailing edge – is found using a standard two-dimensional boundary integral method whose details can be found, for example, in Pozrikidis (2002).

Figures 2 and 3 show, for exactly the same geometry as that used in experiments (see figure 1), the calculated values of the pressure coefficient

$$C_p = \frac{p - p_\infty}{\rho\, U_\infty^2/2} = 1 - \left(\frac{\partial\bar{\phi}}{\partial\,\bar{s}}\right)^2, \tag{2.3}$$

and of the dimensionless pressure gradient $-d\,C_p/d\bar{s}$, with $\bar{s} = s/c$ and $\bar{\phi} = \phi/(U_\infty\, c)$ indicating, respectively, the dimensionless arclength along the airfoil surface and the dimensionless velocity potential; see figure 1(*b*). The results in figure 3 reveal that the sign and the magnitude of the pressure gradient do strongly depend on the position of the injection orifice: for instance, while the pressure gradient is favourable and increases monotonically with the angle of attack for $\bar{x} = x/c = 0$, the pressure gradient changes sign with $\alpha$ for $\bar{x} \ll 1$. The numerical results in figure 3 are confirmed by the experimental evidence in figure 4: here, the process of bubble formation for $\alpha \simeq 12^\circ$ at two neighbouring orifices is illustrated. While bubbles are formed periodically at the injection orifice where the pressure gradient is strongly favourable,

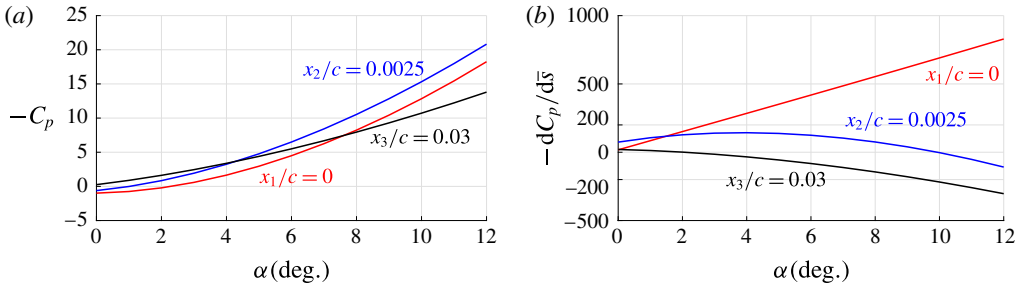


FIGURE 3. (*a*) $C_p$ versus $\alpha$ at the three different locations nearby the leading edge of the airfoil illustrated in figure 4(*b*). (*b*) $\mathrm{d}C_p/\mathrm{d}\bar{s}$ versus $\alpha$ at the same spatial locations as in (*a*).

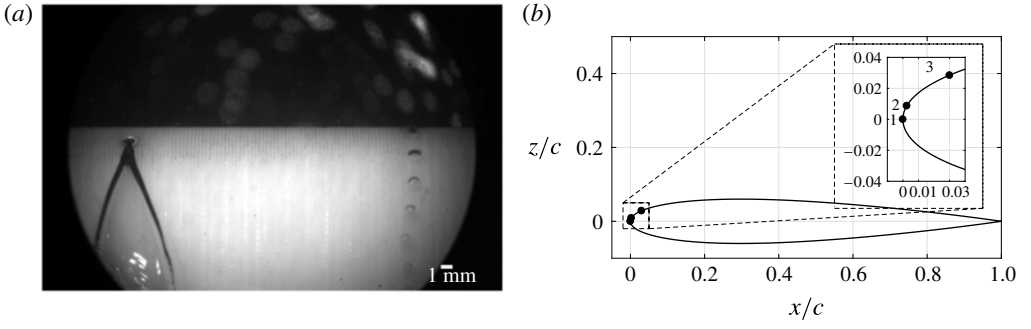


FIGURE 4. (*a*) Production of bubbles at two orifices, located respectively at $\bar{x}_1 = x_1/c = 0$ (right) and at $\bar{x}_2 = x_2/c = 0.0025$ (left) for $\alpha = 11.41°$, $U_\infty = 0.72$ m s$^{-1}$. The production of bubbles is periodic at the orifice located at $\bar{x}_1 = 0$, where the pressure gradient is favourable; however, in contrast, no bubbles are formed at $\bar{x}_2 = 0.0025$, where the pressure gradient is adverse (see figure 3*b*). The scale bar indicates 1 mm. (*b*) Illustration of the spatial locations where the different values of the curves in figure 3 are calculated. This figure shows how close the orifice at the left in panel (*a*) is located to the leading edge of the airfoil; therefore, the sign and the modulus of the pressure gradient is highly dependent on the location of the gas injection orifice.

$-\mathrm{d}\,C_p/\mathrm{d}\bar{s}(\bar{x} = 0) \simeq 800$, no bubbles but a long gas jet is formed at the orifice where the value of the pressure gradient is adverse, $-\mathrm{d}\,C_p/\mathrm{d}\bar{s}(\bar{x} = 0.0025) \simeq -100$ (see figure 3*b*). Indeed, even in the case individual bubbles were formed at the injection orifice at which the pressure gradient is adverse, these bubbles would coalesce because they would be strongly decelerated in the downstream direction as a consequence of the smallness of the gas-to-liquid density ratio.

Therefore, the strategy followed here to produce monodisperse microbubbles is to inject the gas in a region of the flow where $-C_p$ is as large as possible, so that the local pressure $p = p_\infty + (\rho\, U_\infty^2\, C_p(\alpha))/2$ is as small as possible and hence the overpressures needed to make the gas flow through the pipes are as low as possible. In this way, the energy consumption associated with the injection of the gas is clearly reduced with respect to the case in which the local liquid pressure is $\simeq p_\infty$. In addition, in order to minimize the diameters of the bubbles formed, the gas needs to be injected in a region of the flow where the modulus of the favourable pressure gradient is as large as possible; see equation (1.4). These restrictions, together with

| Parameters | Values |
|---|---|
| $U_\infty$ (m s$^{-1}$) | [0.36, 0.5, 0.58, 0.72] |
| $\alpha$ (deg.) | [4.66, 6.23, 8, 9.61, 11.41] |
| $p_g$ (mbar) | [120, 207, 289, 400, 565, 713, 890] |

TABLE 1. Values of the different parameters explored in the present experimental study.

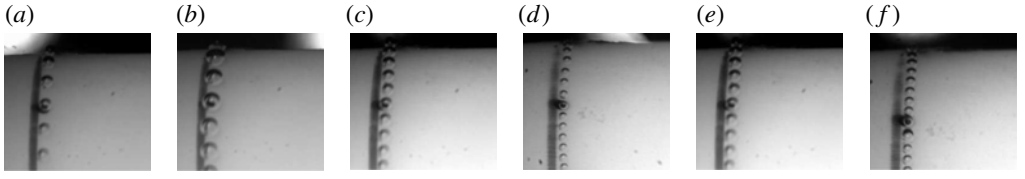


FIGURE 5. (*a*,*b*): Effect of $p_g$ on the diameters of the bubbles generated for $\alpha = 8°$, $U_\infty = 0.58$ m s$^{-1}$. In (*a*), $p_g = 2.07 \times 10^4$ Pa, and in (*b*), $p_g = 7.13 \times 10^4$ Pa. (*c*,*d*): Effect of $U_\infty$ on the diameters of the bubbles generated for $\alpha = 9.61°$, $p_g = 2.07 \times 10^4$ Pa. In (*c*) $U_\infty = 0.36$ m s$^{-1}$ and in (*d*) $U_\infty = 0.58$ m s$^{-1}$. (*e*,*f*): Effect of $\alpha$ on the diameters of the bubbles generated for $U_\infty = 0.5$ m s$^{-1}$, $p_g = 2.89 \times 10^4$ Pa. In (*e*), $\alpha = 4.66°$ and in (*f*), $\alpha = 11.41°$.

the evidence depicted in figures 3 and 4, suggest that the appropriate location to produce the bubbles is the leading edge of the airfoil. Consequently, from now on, we will limit ourselves to analyse the production of bubbles from orifices located at $\bar{x} = 0$ for the range of experimental parameters shown in table 1.

Figure 5 shows the influence of $\alpha$, $Q_g$ and $U_\infty$ on the bubble generation process. As is expected from (1.4) and from the results shown in figure 3, figure 5 reveals that the diameters of the bubbles formed decrease for increasing values of $\alpha$ and $U_\infty$ and decreasing values of $Q_g$ – or, equivalently, of the gas pressure in the reservoir, $p_g$. The qualitative observations depicted in figure 5 are quantified in figure 6, where both $f_b$ and $d_b$ are shown for the values of the parameters in table 1. The exhaustive analysis of the experimental data yields values of the PDI below 0.05; therefore, the bubbles produced using our method are monodisperse (Rodríguez-Rodríguez *et al.* 2015).

In order to rationalize the experimental observations in figure 6, where the bubbling frequencies seem to be randomly distributed, notice first that, for the case of the flow around the airfoil, the local pressure gradient is

$$|\nabla p| = \beta(\alpha)\frac{\rho\, U_\infty^2}{c} \gg \frac{\rho\, U_\infty^2}{c}, \tag{2.4}$$

with

$$\beta(\alpha) = -\frac{1}{2}\frac{\mathrm{d}C_p}{\mathrm{d}\bar{s}}(\alpha, x/c = 0), \tag{2.5}$$

and $-\mathrm{d}C_p/\mathrm{d}\bar{s}$ given by the red curve in figure 3(*b*). Therefore, making use of equations (1.3) and (1.4) we expect that, if condition (1.5) is satisfied, the bubbling frequencies and the bubble diameters can be expressed as a function of the control parameters as

$$f_b = K_{f1}\left(\frac{U_\infty}{\sqrt{c\, d_b/\beta(\alpha)}}\right) \quad \text{and} \quad \frac{d_b}{L} = K_{b1}\left(\frac{Q_g}{U_\infty L^2\sqrt{L\,\beta(\alpha)/c}}\right)^{2/5}, \tag{2.6a,b}$$

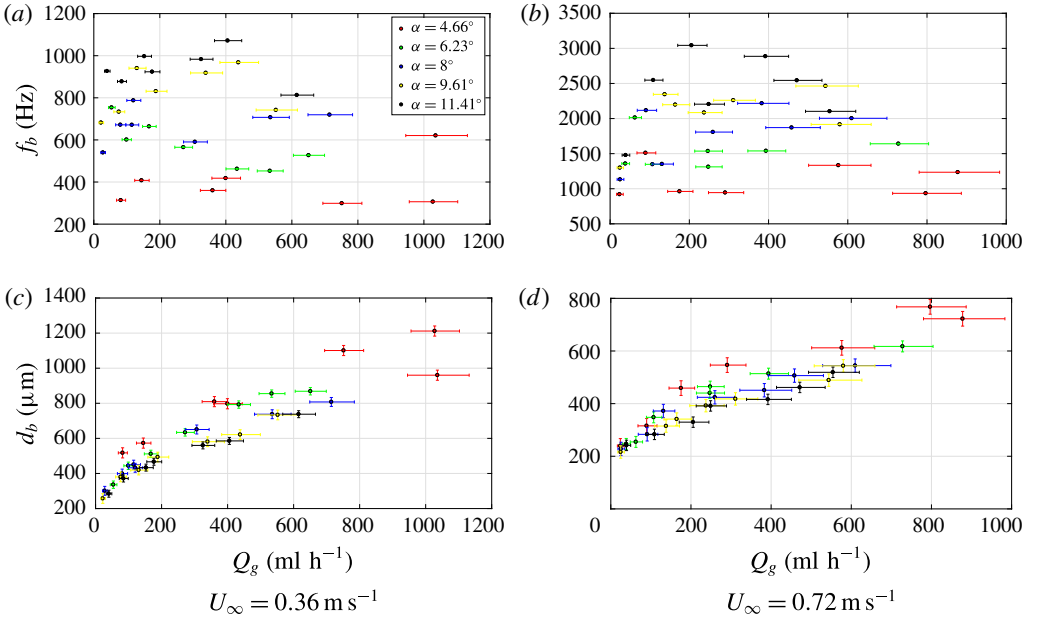


FIGURE 6. (*a*,*b*) Bubbling frequencies for two different values of the incident velocity. (*c*,*d*) Diameters of the bubbles generated corresponding to the bubbling frequencies depicted in (*a*) and (*b*), respectively.

with $L = 10^{-3}$ m the same length scale as in Evangelio, Campo-Cortés & Gordillo (2015) and $K_{f1}$ and $K_{b1}$ constants. However, if condition (1.5) is not satisfied, namely, if

$$K_{b1}\left(\frac{Q_g}{U_\infty L^2\sqrt{L\,\beta(\alpha)/c}}\right)^{2/5} \lesssim K\left(\frac{\sigma}{\nabla p\, L^2}\right)^{1/2}, \tag{2.7}$$

with $K = 0.56$ an experimentally determined constant, $f_b$ and $d_b$ are expected to be given by (see (1.6))

$$f_b = K_{f2}\frac{U_\infty(1-C_p)^{1/2}}{d_t} \quad \text{and} \quad \frac{d_b}{L} = \left(\frac{6\,d_t}{K_{f2}\pi\,L}\right)^{1/3}\left(\frac{Q_g}{U_\infty L^2(1-C_p)^{1/2}}\right)^{1/3}, \tag{2.8a,b}$$

where the local velocity at the spatial location where the gas is injected, $U$, has been calculated using the definition of the pressure coefficient in (2.3):

$$U = U_\infty(1-C_p)^{1/2}. \tag{2.9}$$

The value $K = 0.56$ in (2.7) is the one minimizing the dispersion of the experimental data with respect to the values predicted in equations (2.6) and (2.8). Indeed, the results obtained for $K = 0.56$, depicted in figure 7, show that the predictions for $f_b$ and $d_b/L$ in (2.6), are in fair agreement with the experimental measurements when the values $K_{f1} = 1.8$ and $K_{b1} = 1.02$, given in Evangelio *et al.* (2015), are used. For those cases in which the condition (2.7) is verified (i.e. when the value of the

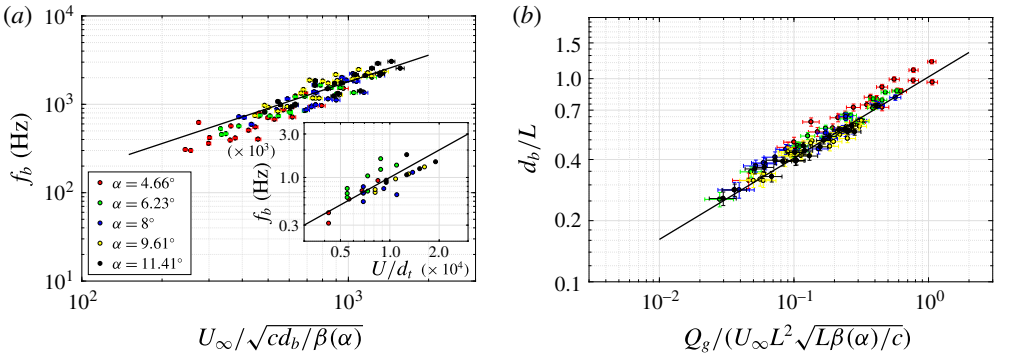


FIGURE 7. (*a*) Comparison between the bubbling frequencies predicted in (2.6) and experiments. The inset represents the comparison between the bubbling frequencies predicted in (2.8) and the few experimental data verifying the condition (2.7). (*b*) The experimental values of the bubble diameters not verifying (2.7) are in fair agreement with the scaling for $d_b/L$ given in (2.6). The diameters of the bubbles corresponding to those experimental conditions for which (2.7) is verified, namely, those experiments for which the role played by interfacial tension stresses in the bubble formation process can no longer be neglected, are not included here.

local Bond number defined in (1.5) is low enough and, therefore, the role played by capillary stresses in the bubble formation process can no longer be neglected), the inset in figure 7(*a*) also reveals a fair agreement between the predicted frequency in (2.8) and the experimental data for $K_{f2} = 0.1$, a value which is very close to that reported in Campo-Cortés *et al.* (2016). Let us emphasize that the agreement between measurements and the predictions in (2.6)–(2.8) depicted in figure 7 has been obtained using already reported values for the constant in microfluidic geometries and using the values of the pressure gradients and local velocities calculated numerically. These facts indicate that the bubble generator presented here is, in essence, the same as those reported using microfluidics, in spite of the evident geometrical differences.

Equations (2.6) and (2.8) predict the precise way the bubble diameter $d_b$ decreases when $Q_g$ is decreased or the values of both $U_\infty$ and $\alpha$ are increased. In particular, equations (2.6) and (2.8) indicate that, for fixed values of $\alpha$ and $Q_g$, $d_b$ could have been decreased below the minimum bubble diameter reported in this study ($\simeq$200 μm), if the maximum liquid velocity in the water tunnel could have been increased above $\simeq$0.7 m s$^{-1}$.

However, the validity of the strategy described above to decrease the diameters of bubbles generated, using the procedure presented here, possesses one clear limitation that prevents increasing $U_\infty$ without bound: liquid cavitation. Indeed, the gas is injected in a region of the flow where the pressure is $p \simeq p_a + \rho\, U_\infty^2\, C_p(\alpha)/2$, with $C_p(\alpha) < 0$ and $p_\infty \simeq p_a$, where $p_a \simeq 10^5$ Pa is the atmospheric pressure. Therefore, $p$ could be so low for sufficiently large values of $U_\infty$ that vapour bubbles could be nucleated. The description of the interaction of the gas bubbles produced with the vapour bubbles that would be nucleated at the leading edge region of the airfoil for sufficiently large values of the incident velocity $U_\infty$ is left for a future study.

## 3. Conclusions

In this contribution we have presented a method for producing monodisperse microbubbles avoiding the use of microchannels. This method consists in injecting a given gas flow rate at the leading edge of an airfoil placed at an angle of attack $\alpha$ inside a liquid stream. In this region of the airfoil, the liquid velocities and the pressure gradients are much higher than $U_\infty$ and $\rho U_\infty^2/c$, respectively, a fact favouring the generation of monodisperse microbubbles with diameters and frequencies identical to those found in microfluidic geometries. The advantage of the present method with respect to the ones reported in the literature is that the flow through microchannels, prone to clogging, not straightforwardly scalable for mass production in real applications and involving large pressure losses, is avoided. One of the possible ways to upscale the production of monodisperse microbubbles from a single orifice would be to inject the gas at the leading edge of blades rotating at an angular frequency below the one at which liquid cavitation occurs.

In summary, this contribution presents a feasible method that could help change the paradigmatic idea that microfluidics is the only way of producing uniformly sized micron-sized bubbles or drops in a controllable way.

## Acknowledgements

This study has been financially supported by the Spanish MINECO under Projects DPI2014-59292-C3-2-P, DPI2017-88201-C3-1-R and DPI2015- 71901-REDT, partly financed through European funds and also with funding from Vicerrectorado de Investigación, Universidad de Sevilla. We are grateful to C. Martínez-Bazán, J. Rodríguez-Rodríguez and A. Sevilla for their encouraging comments.

## References

Abbot, I. H. & Von Doenhoff, A. E. 1959 *Theory of Wing Sections. Including a Summary of Airfoil Data*. Dover.

Campo-Cortés, F., Riboux, G. & Gordillo, J. M. 2016 The effect of contact line pinning favors the mass production of monodisperse microbubbles. *Microfluid. Nanofluid.* **20**, 21.

Eggers, J. & Villermaux, E. 2008 Physics of liquid jets. *Rep. Prog. Phys.* **71** (3), 036601.

Evangelio, A., Campo-Cortés, F. & Gordillo, J. M. 2015 Pressure gradient induced generation of microbubbles. *J. Fluid Mech.* **778**, 653–668.

Ferrara, K., Pollard, R. & Borden, M. 2007 Ultrasound microbubble contrast agents: fundamentals and application to gene and drug delivery. *Annu. Rev. Biomed. Engng* **9**, 415–447.

Fu, T. & Youguang, M. 2015 Bubble formation and breakup dynamics in microfluidic devices: a review. *Chem. Engng Sci.* **135**, 343–372.

Gañán-Calvo, A. M. & Gordillo, J. M. 2001 Perfectly monodisperse microbubbling by capillary flow focusing. *Phys. Rev. Lett.* **87**, 274501.

Garcia-Ochoa, F. & Gomez, E. 2009 Bioreactor scale-up and oxygen transfer rate in microbial processes: an overview. *Biotechnol. Adv.* **27** (2), 153–176.

Garstecki, P., Gitlin, I., Diluzio, W., Whitesides, G. M., Kumacheva, E. & Stone, H. A. 2004 Formation of monodisperse bubbles in a microfluidic flow-focusing device. *Appl. Phys. Lett.* **85**, 2649–2651.

Gordillo, J. M., Sevilla, A. & Martínez-Bazán, C. 2007 Bubbling in a co-flow at high Reynolds numbers. *Phys. Fluids* **19** (7), 1–18.

Hettiarachchi, K., Talu, E., Longo, M. L., Dayton, P. A. & Lee, A. P. 2007 On-chip generation of microbubbles as a practical technology for manufacturing contrast agents for ultrasonic imaging. *Lab on a Chip* **7**, 463–468.

OGUZ, H. N. & PROSPERETTI, A. 1993 Dynamics of bubble-growth and detachment from a needle. *J. Fluid Mech.* **257**, 111–145.

POZRIKIDIS, C. 2002 *A Practical Guide to Boundary Element Methods with the Software Library BEMLIB*. CRC Press.

RODRÍGUEZ-RODRÍGUEZ, J., SEVILLA, A., MARTÍNEZ-BAZÁN, C. & GORDILLO, J. M. 2015 Generation of microbubbles with applications to industry and medicine. *Annu. Rev. Fluid Mech.* **47** (September), 405–429.

ROSSO, D., LARSON, L. E. & STENSTROM, M. K. 2008 Aeration of large-scale municipal wastewater treatment plants: state of the art. *Water Sci. Technol.* **57** (7), 973–978.

SHIROTA, M., SANADA, T., SATO, A. & WATANABE, M. 2008 Formation of a submillimeter bubble from an orifice using pulsed acoustic pressure waves in gas phase. *Phys. Fluids* **20** (4), 043301.

VILLERMAUX, E. 2007 Fragmentation. *Annu. Rev. Fluid Mech.* **39** (1), 419–446.

YOSHIZAWA, S., IKEDA, T., ITO, A., OTA, R., TAKAGI, S. & MATSUMOTO, Y. 2009 High intensity focused ultrasound lithotripsy with cavitating microbubbles. *Med. Biol. Engng Comput.* **47** (8), 851–860.

ZIMMERMAN, W. B., ZANDI, M., HEMAKA BANDULASENA, H. C., TESA, V., JAMES GILMOUR, D. & YING, K. 2011 Design of an airlift loop bioreactor and pilot scales studies with fluidic oscillator induced microbubbles for growth of a microalgae *Dunaliella salina*. *Appl. Energy* **88** (10), 3357–3369.